Broadband and Omnidirectional Anti-Reflection Coating for III/V Multi-Junction Solar Cells

Silke L. Diedenhofen, Gabriele Vecchi, Gerard Bauhuis, and Jaime Gómez Rivas

Abstract Graded refractive index layers reduce the reflection and increase the coupling of light into a substrate by optical impedance matching at the interfaces. Due to the optical impedance matching, reflections at the interfaces are not possible for a broad wavelength range, rendering this type of anti-reflection coating a promising candidate for III/V multi-junction solar cells. Graded refractive index layers can be modeled using a transfer-matrix method for isotropic layered media. We derive the transfer-matrix method and we show calculations of the reflection from and the transmission into an AlInP layer coated with different anti-reflection coatings. We describe a new type of anti-reflection coating based on tapered semiconductor nanowires and we show reflection and transmission measurements of those kind of anti-reflection coatings on top of different substrates.

Silke L. Diedenhofen
ICFO - The Institute of Photonic Sciences, Av. Carl Friedrich Gauss, 3, 08860 Castelldefels (Barcelona), Spain e-mail: silke.diedenhofen@icfo.es

Gabriele Vecchi
FOM Institute AMOLF, c/o Philips Research Laboratories, High-Tech Campus 4, 5656 AE Eindhoven, The Netherlands

Gerard Bauhuis
Radboud University Nijmegen, Institute for Molecules and Materials, Applied Materials Science, Heyendaalseweg 135, 6525 AJ Nijmegen, The Netherlands e-mail: G.Bauhuis@science.ru.nl

Jaime Gómez Rivas
FOM Institute AMOLF, c/o Philips Research, High-Tech Campus 4, 5656 AE Eindhoven, Applied Physics, Photonics & Semiconductor Nanophysics, Eindhoven University of Technology, 5600 MB Eindhoven, The Netherlands e-mail: rivas@amolf.nl

1 Introduction

Photovoltaic research has provided many solutions to increase the efficiency of solar cells [12]. Triple junction solar cells with efficiencies exceeding 40 % have already been demonstrated [20, 13]. These triple junction solar cells have a germanium cell at the bottom, a GaAs middle cell, and a InGaP cell at the top and because of their monolithic structure, the current of the solar cell is limited by the lowest current generated in one of the subcells. The bandgap energy of Ge is low and Ge absorbs light of a broad range of wavelengths, resulting in a current in this cell that exceeds the current in the GaAs and InGaP subcells, in which light in a narrower wavelength range is absorbed. Therefore, the anti-reflection coating for this type of solar cells has to be optimized for the wavelength range in which InGaP and GaAs are absorbing, i.e., 300 nm to 875 nm. For longer wavelengths, the reflection losses are less critical.

Nowadays, research is focusing on the realization of quadruple solar cells [30]. Quadruple solar cells have expected efficiencies exceeding 50 % [19]. A schematic of a possible quadruple solar cell is given in Figure 1a. In this example, the solar cell consists of four different subcells, where the medium with the highest electronic bandgap energy forms the top subcell, for example, InGaP. Below the top subcell, GaAs, InGaAsP, and InGaAs subcells are fabricated, each absorbing the light of a spectral energy lower than the one above. The top-most layer of the solar cell is an AlInP window layer for passivation of the InGaP cell. In this example the quadruple cell consists of two mechanically stacked tandem cells. Both tandem cells are grown lattice matched, the first two subcells on GaAs and the last two subcells on InP [23].
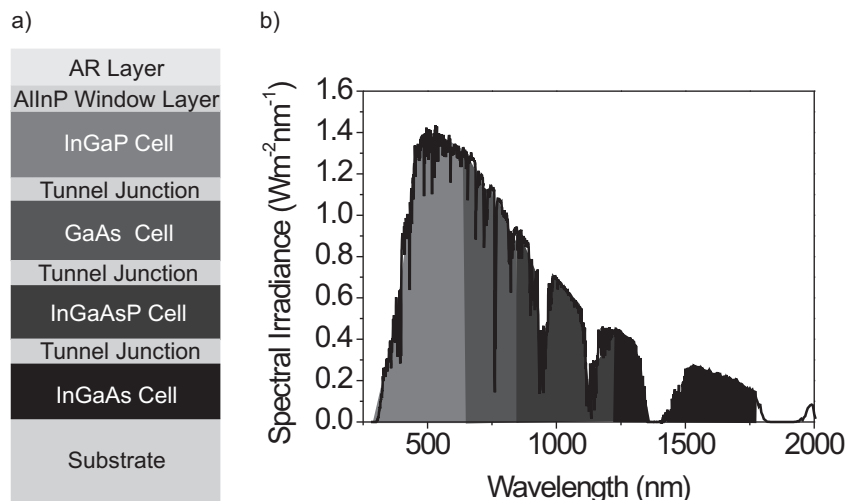

Fig. 1 a) Schematic of a quadruple solar cell and b) Solar spectrum AM1.5D and absorption band of the individual junctions of the quadruple solar cell.

In these quadruple solar cells, each subcell absorbs nearly the same amount of photons. To show the wide spectral range that can be covered with multi-junction solar cells, Figure 1b shows the solar irradiance standard AM1.5D, including the absorption bands of a quadruple-junction solar cell. Therefore, this type of solar cell requires an anti-reflection coating that covers a wavelength range from 300 nm to 1700 nm [19]. The MgF_2/ZnS double layer anti-reflection coatings that are used for III/V single junction solar cells are not sufficient for reducing the reflection over the broad wavelength range that is absorbed by the multiple junctions [30, 9]. Broadband anti-reflection layers are necessary to approach an optimal performance and the maximum efficiency that has been theoretically calculated. The spectral range of an anti-reflection coating is not the only factor limiting the efficiency of multi-junction solar cells. As these solar cells will be mainly installed in solar concentrator systems, the angular response has to be optimized as well.

Anti-reflective layers can be classified into two different types: I) homogeneous layers or step index layers and II) inhomogeneous layers or graded index layers [8]. Step-index layers reduce the reflection due to destructive interference of light reflected at different interfaces [2]. The working principle of the step index layers is illustrated in Figure 2a. The fabrication of single anti-reflection layers is well known for decades [21], but the layer thickness and material have to be chosen carefully for each wavelength, angle, and substrate. The bandwidth of these coatings is lower than one octave, for example 400-700 nm or 800-1100 nm and the angle of incidence is limited to 30° [15]. In contrast to step index layers, graded refractive index layers reduce the reflection due to a gradually increasing refractive index from the top to the bottom. This gradual increase of the refractive index leads to optical impedance matching at the interfaces and does not allow for reflections (see Figure 2b). Graded refractive index coatings have been extensively studied theoretically [28, 29, 8, 27, 11]. Southwell found that an optimum anti-reflection coating that reduces the reflection from glass should have a refractive index distribution along its thickness that follows a quintic function, that is a polynomial with degree 5. [29]. Dobrowolski et al. provide an extensive comparison of different homogeneous and graded refractive index coatings and further investigate different types of quintic refractive index profiles [8, 27]. Theoretically, a drastic reduction of the reflection for angles up to 80° and for a wavelength range of one order of magnitude is possible, for example from 400 nm to 4 μm [27].

Since Bernhard reported in 1967 that the eyes of moths are covered with nanostructures that improve the light coupling [1], the effect of these nanostructures has been investigated intensely [5, 22, 10, 17, 18, 41, 25, 24, 37, 16, 32, 31, 40, 4, 42, 38]. Nanostructures improve the light coupling into the eyes of night-seeing moths by forming a layer with graded refractive index varying from a value close to 1 at the air-nanostructure interface to the refractive index of the eye. While it was known that graded refractive index coatings can reduce the reflection and therefore improve the coupling efficiency into high index materials, fabrication of layers with a refractive index close to the refractive index of air remained challenging. Nowadays, nanostructuring techniques allow the fabrication of subwavelength structures
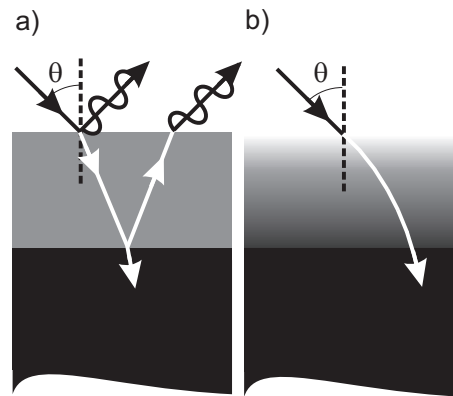
Fig. 2 a) Step index anti-reflection layers reduce the reflection due to destructive interference of light reflected at different interfaces. b) Graded index coatings refract the light gradually into the substrate without allowing for reflections. (Fig. reproduced from [7].)

which exhibit a very low effective refractive index when packed densely together. A complete review about nanostructured anti-reflection coatings is given in Ref. [3].

Recently, Xi et al. demonstrated a graded refractive index structure that was fabricated in a bottom-up process using SiO_2 and TiO_2 nanowires. These nanowires were fabricated by oblique-angle depositions on AlN [37]. The graded refractive index structure was achieved by varying the filling fraction of nanowires from one layer to the next, and by changing the material from a low refractive index material at the top (SiO_2) to a material with a higher refractive index at the bottom (TiO_2). Therefore, the evaporation of two materials is necessary for these coatings. Lee et al. employed a different bottom-up approach based on chemical vapor deposition. Using this technique, they have demonstrated anti-reflection coatings consisting of single materials [24]. These coatings are formed by ZnO nanowires grown on a Si substrate. Transmission measurements for visible wavelengths have not been possible because of the silicon substrates [24], and the effects of light scattering by the nanowires on the reduction of the reflection could not be determined. Further, the reflection from Si substrates has been reduced by etching different kinds of nanostructures into the substrate with top-down nanostructuring processes [16, 32, 31, 40]. With these etching techniques, very low values of the specular reflection have been reported. However, it has not been unambiguously demonstrated whether this reduced reflection occurs due to light scattering by the nanostructures, to an enhanced absorption in the anti-reflection layer, to refractive index matching to the substrate, or to a combination of these phenomena. An important limitation of etched silicon surfaces is that the anti-reflection layer is also absorbing. The fabrication of nonabsorbing anti-reflection layers on top of absorbing substrates is thus impossible by etching.

We describe in this chapter bottom-up grown tapered GaP nanowires forming a broadband and omni-directional anti-reflection coating [7, 6]. The bottom-up growth method used for fabricating nanowires allows hetero-epitaxial growth, that is the growth of different materials with different crystal structure on top of each other. Therefore, this technique provides the possibility for growing a passive anti-reflection layer on top of the active layer of the solar cell. Having a passive, non-

absorbing anti-reflection layer is advantageous because of the following reasons: Surface carrier recombination can be dominant in active, absorbing nanostructured materials due to their large surface-to-volume-ratio. This effect is not relevant in the case of passive nanostructures, such as the proposed anti-reflection nanowire layers, since light is not absorbed in these structures. Carriers are only generated in the active multi-junction solar cell, beneath the nanowire coating, where they can be separated and extracted.While it has been proposed that a modified quintic refractive index profile can provide the largest reduction of the reflection, fabrication of modified index profiles using nanowires is not trivial. A quadratic index profile from conical nanowires is expected, since the refractive index is proportional to the nanowire filling fraction and the filling fraction scales with the area.

The aim of this chapter is to provide an introduction to graded-refractive index coatings that are based on tapered GaP nanowires. In Section 2 we introduce the transfer matrix method that is used to calculate the transmission through and reflection from multi-layer systems. We compare calculations of the photocurrent densities of III/V quadruple solar cells covered with different anti-reflection coatings. These calculations have revealed that a graded refractive index layer increases the photocurrent density of the solar cell with respect to a solar cell coated with a standard MgF_2/ZnS double layer anti-reflection coating [6]. We describe in Section 3 the vapor-liquid-solid growth of tapered GaP nanowires on GaP and AlInP/GaAs substrates. Further, we explain the anti-reflective behavior of GaP nanowires on top of a GaP substrate. We show transmittance and reflectance measurements that have unambiguously demonstrated that tapered GaP nanowires form an anti-reflection coating [7]. We end the chapter with a description of the anti-reflective behavior of tapered GaP nanowires on an AlInP/GaAs substrate [6]. The anti-reflective behavior of these nanowires constitute a proof-of-principle as they are the first experimental verification that tapered GaP nanowires could be used as an anti-reflection layer for III/V solar cells.

2 Transfer Matrix Method

The transfer matrix method can be used for modeling graded refractive index layers [39]. In this section, we shortly introduce this method. Let us consider a three layer system as the one depicted in Figure 3. The electric field amplitude of an electromagnetic plane wave of angular frequency ω propagating with the z-component of the wavevector k_z in the xz plane is given by

$$\mathbf{E} = \mathbf{E}(x)e^{i(\omega t - k_z z)}. \tag{1}$$

Further, we assume that the light is linearly polarized, either s-polarized, i.e., $\mathbf{E} \parallel \mathbf{y}$ or $E_x = E_z = 0$, or p-polarized, i.e., $\mathbf{H} \parallel \mathbf{y}$ or $E_y = 0$. If we assume that light is only impinging on the three layer system from medium 1, the electric field in layer 1 and 2 consists of a right- and left-traveling wave and can be written as

Fig. 3 A three layer system consisting of three materials with refractive indices n_1, n_2, and n_3, respectively. The field amplitudes at the interfaces are given by a_1, a_2', a_2, a_3', for the right traveling waves and b_1, b_2', b_2, b_3' for the left traveling wave. The incident light beam with the wavevector **k** and the angle of incidence θ_1 is defined in medium 1.
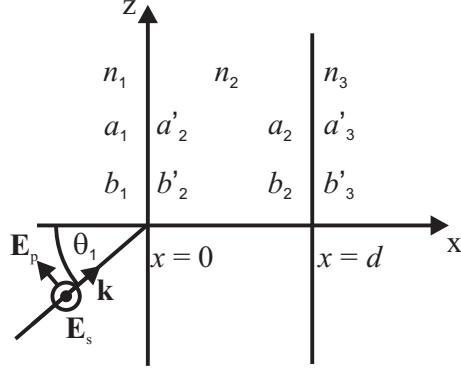
$$E(x) = a\mathrm{e}^{-ik_{\mathrm{x}}x} + b\mathrm{e}^{ik_{\mathrm{x}}x} \equiv a(x) + b(x), \tag{2}$$

where $\pm k_{\mathrm{x}}$ are the x-components of the wave vector given by $k_{\mathrm{x}} = n_\alpha \frac{2\pi}{\lambda}\cos\theta_\alpha$ in medium α with refractive index n_α, angle inside the medium θ_α, and at vacuum wavelength λ. The field amplitudes a and b are constant in each homogeneous layer. The amplitude of the wave traveling to the right is represented by $a(x)$, while the left traveling component is described by $b(x)$. We define the various amplitudes at the interfaces between the different media as

$$
\begin{aligned}
a_1 &= a(0^-),\\
b_1 &= b(0^-),\\
a_2' &= a(0^+),\\
b_2' &= b(0^+),\\
a_2 &= a(d^-),\\
b_2 &= b(d^-),\\
a_3' &= a(d^+),\\
b_3' &= b(d^+) = 0,
\end{aligned}
\tag{3}
$$

where 0^- represents the left side and 0^+ the right side of the interface at $x = 0$, and d^- and d^+ represent the left and right side of the interface at $x = d$ (see Fig. 3). If we represent the left and right traveling components of the electric field as column vectors, the vectors at each side of the interface are related by

$$\begin{pmatrix} a_1 \\ b_1 \end{pmatrix} = \mathbf{D}_{1,2}\begin{pmatrix} a_2' \\ b_2' \end{pmatrix}, \tag{4}$$

$$\begin{pmatrix} a_2' \\ b_2' \end{pmatrix} = \mathbf{P}_2\begin{pmatrix} a_2 \\ b_2 \end{pmatrix}, \tag{5}$$

$$\begin{pmatrix} a_2 \\ b_2 \end{pmatrix} = \mathbf{D}_{2,3} \begin{pmatrix} a'_3 \\ b'_3 \end{pmatrix} \tag{6}$$

where $\mathbf{D}_{1,2}$, and $\mathbf{D}_{2,3}$ are the so-called transmission matrices and $\mathbf{P}_2$ is the propagation matrix that accounts for the propagation in the layer. The matrices are defined for layer α as follows:

$$\mathbf{D}_{\alpha,\alpha+1} = \frac{1}{t_{\alpha,\alpha+1}} \begin{pmatrix} 1 & r_{\alpha,\alpha+1} \\ r_{\alpha,\alpha+1} & 1 \end{pmatrix} \tag{7}$$

and

$$\mathbf{P}_\alpha = \begin{pmatrix} e^{i\phi_\alpha} & 0 \\ 0 & e^{-i\phi_\alpha} \end{pmatrix}, \tag{8}$$

where $t_{\alpha,\alpha+1}$ and $r_{\alpha,\alpha+1}$ are the Fresnel amplitude transmission and reflection coefficients for the interface [2] and $\phi_\alpha = \frac{2\pi}{\lambda} n_\alpha \cos\theta_\alpha L$ is the phase change of light traveling through the layer, with L the thickness of the layer.

From Equations (4)-(6), the amplitudes a_1, b_1, and a'_3 and b'_3 are related by the multiplication of the transmission matrix and the propagation matrix

$$\begin{aligned} \begin{pmatrix} a_1 \\ b_1 \end{pmatrix} &= \mathbf{D}_{1,2} \mathbf{P}_2 \mathbf{D}_{2,3} \begin{pmatrix} a'_3 \\ b'_3 \end{pmatrix} \\ &= \begin{pmatrix} M_{11} & M_{12} \\ M_{21} & M_{22} \end{pmatrix} \begin{pmatrix} a'_3 \\ b'_3 \end{pmatrix} \\ &= \mathbf{M} \begin{pmatrix} a'_3 \\ b'_3 \end{pmatrix}. \end{aligned} \tag{9}$$

The multiplication of the matrices can be represented by the transfer matrix $\mathbf{M}$ consisting of the four elements M_{11}, M_{12}, M_{21}, and M_{22}.

The reflection and transmission of a plane wave through the three layer structure for light coming from layer 1 are defined as

$$r = \left(\frac{b_1}{a_1} \right)_{b'_3 = 0}, \tag{10}$$

and

$$t = \left(\frac{a'_3}{a_1} \right)_{b'_3 = 0}, \tag{11}$$

respectively, where b'_3 is set to 0 as there is not a traveling wave from right to left in medium 3. Using Equation (9), the amplitude reflection and transmission coefficients of the layered system are given by

$$r = \frac{M_{21}}{M_{11}} \tag{12}$$

and

$$t = \frac{1}{M_{11}}. \tag{13}$$

The reflectance R for the case that the medium of layer 1 is lossless is defined as

$$R = |r|^2 = \left| \frac{M_{21}}{M_{11}} \right|^2. \tag{14}$$

If the bounding layers, 1 and 3, are both dielectrics, with real n_1 and n_3, the transmission T for a wave indicent with an angle θ_1 is given by

$$T = \frac{n_3 \cos \theta_3}{n_1 \cos \theta_1} |t|^2 = \frac{n_3 \cos \theta_3}{n_1 \cos \theta_1} \left| \frac{1}{M_{11}} \right|^2, \tag{15}$$

with θ_3 the angle the light forms with the x axis in the third layer related to θ_1 by Snell's law.

Fig. 4 The graded refractive index of conical nanowires is modeled by "slicing" the nanowire layer into sublayers, each having a slightly increased refractive index than the layer before, indicated by the gradient in color.
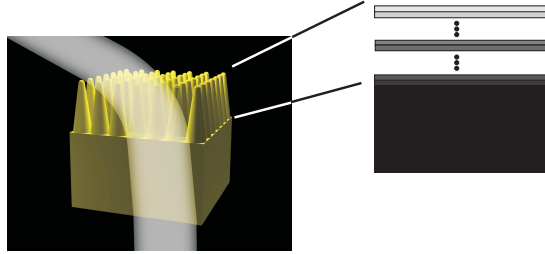
While we have explained above the transfer-matrix method for three layers, the formalism for a multi-layer structure can be easily deduced by multiplying the transmission and propagation matrices for each layer involved. For modeling the graded refractive index of the nanowire layer, the nanowire layer is "sliced" into sublayers with a thickness much small than the wavelength and each having a slightly increased refractive index with respect to the preceding layer. This slicing of the layers is illustrated in Figure 4. In this schematic, the gradient in color represents a change in refractive index.

2.1 Comparison of Different Anti-reflection Layers

It has been shown in Ref. [6] that graded refractive index anti-reflection coatings can increase the bandwidth of reduced reflection compared to double layer antireflection coatings. Therefore, the reflection from and transmission through an AlInP window layer on top of an infinitely thick GaAs substrate coated with MgF$_2$/ZnS double layer anti-reflection coating and graded refractive index anti-reflection coatings with different thicknesses have been calculated. Figure 5 displays the reflectance in a linear and logarithmic scale (inset), calculated using the transfer matrix method from

an AlInP layer with a thickness of 30 nm on top of an infinitely thick GaAs substrate coated with different anti-reflection layers. In these calculations, the refractive index of AlInP varies from 3.06 - 2.14i at 350 nm to 2.77 at 1700 nm, and the refractive index of GaAs from 3.28 - 2.06i at 350 nm to $3.36 - 5.32 \cdot 10^{-5}$i at 1700 nm. These values had been determined from ellipsometry measurements on the materials used in the experiments shown in the next section. The refractive indices of ZnS and MgF$_2$ vary between 2.8 - 0.13i and 2.27, and between 1.38 - 1.37, respectively, for wavelengths in the range 350 nm to 1700 nm. The black solid curves in Figure 5a show the calculated reflectance of the bare AlInP/GaAs layers without an anti-reflection coating. The reflectance from the AlInP/GaAs layers coated with a MgF$_2$/ZnS double layer anti-reflection coating with thicknesses of 89 nm (ZnS) and 105 nm (MgF$_2$) is displayed by the red long-dashed curves in Figures 5a. The calculated reflectance from the AlInP/GaAs layers coated with the MgF$_2$/ZnS anti-reflection coating is lower than 10 % for wavelengths between 450 nm and 1700 nm. This anti-reflection coating reduces the reflection for a rather broad wavelength range, but the bandwidth is not optimal for reducing the reflectance over the wavelength range in which III/V multi-junction solar cells absorb light.

Further, Figure 5a displays calculations of the reflectance from a 30 nm thin AlInP layer on top of an infinitely thick GaAs substrate that is coated with three lossless graded refractive index layers with different thicknesses. These calculations have been performed by "slicing" the graded refractive index layers into sublayers, according to Figure 4. The refractive index of these layers is parabolically increasing from 1.0 to 3.3, and the thicknesses of the layers are 250 nm, 500 nm, and 1000 nm, respectively. The anti-reflection layer has been implemented in the transfer-matrix calculation by considering sublayers with a thickness of 10 nm. These calculations are displayed in Figure 5a by the olive-short-dashed (250 nm), the blue dash-dotted (500 nm), and the magenta dashed-dot-dotted curves (1000 nm), respectively. The graded refractive index layer with a thickness of 250 nm does not decrease the reflectance significantly for wavelengths longer than 850 nm, but the reflectance of the graded refractive index layers with a thickness of 500 nm and 1000 nm are around 1 % or lower for a broad wavelength range. When a 1000 nm thick graded refractive index anti-reflection coating is applied to the AlInP/GaAs layers, the reflection is the lowest. In this coating, the gradient of the refractive index between adjacent sublayers is the smallest.

Analogous to the reflectance calculations, calculations of the transmittance through a 30 nm thin AlInP layer on top of an infinitely thick GaAs substrate coated with the same anti-reflection layers as above have been performed. For these calculations, only the real part of the refractive index of GaAs has been considered. The calculated transmittance is shown in Figure 5b in linear scale The inset of Figure 5b shows a zoom-in to highlight the differences of the coatings. The solar spectrum weighted transmittance *SSWT* has been determined from the calculated transmittance of the different layers by

$$SSWT = \frac{\int F(\lambda) \cdot T(\lambda) d\lambda}{\int F(\lambda) d\lambda}, \tag{16}$$
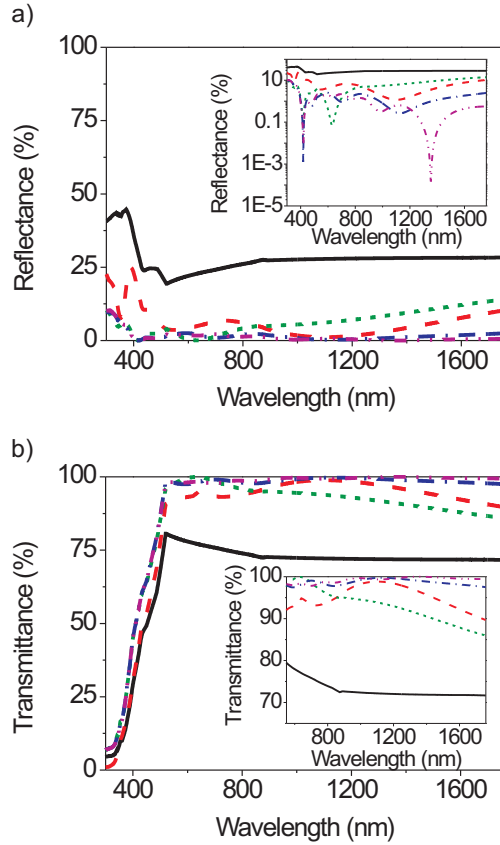
a)

b)

Fig. 5 a) Calculation of the reflectance from and b) transmittance through a 30 nm thin AlInP layer on top of an infinitely thick GaAs substrate coated with different anti-reflection layers in linear scale and logarithmic scale (inset of a)). The black solid curves correspond to the reflectance and transmittance of a bare AlInP layer. The AlInP layer is coated with a MgF_2/ZnS anti-reflection coating with thicknesses of 89 nm (ZnS) and 105 nm (MgF_2) (red dashed curves), a parabolically increasing refractive index layer from 1.0 to 3.3 with a thickness of 250 nm (olive short-dashed curves), 500 nm (blue dash-dotted curves), and 1 μm (magenta dash-dot-dotted curves). The inset of b) shows a zoom-in of the calculation of the transmittance. (Figures reproduced from [6].)

where $F(\lambda)$ and $T(\lambda)$ are the photon flux (AM1.5G, 1000 W/m^2) and the calculated transmittance, respectively. The integration has been performed in the wavelength range from 300 nm to 1760 nm. The solar weighted transmittances of the 5 different samples are 69.2 % for a bare solar cell, 86.3 % for the MgF_2/ZnS anti-reflection coating, 89 % for the 250 nm thick graded refractive index layer, 91.5 % for the 500 nm thick graded refractive index layer, and 91.7 % for the 1 μm thick graded refractive index layer. Therefore, the solar weighted transmittance can be increased by 6.3 % when the 1 μm thick graded refractive index layer is used as an anti-reflection layer instead of the double layer MgF_2/ZnS coating.

Using the transfer matrix method, the reflectance from and transmittance through each individual layer of a III/V multi-junction solar cell have been calculated [14]. For these calculations the III/V solar cell consisted of InGaP, GaAs, InGaAsP, and InGaAs with electronic bandgaps that correspond to cut-off wavelengths of respectively 649 nm, 873 nm, 1215 nm, and 1770 nm. From these values of transmittance and reflectance the absorption in each sublayer has been determined. Multiplying the absorption in each subcell by the photon flux results in the amount of photons absorbed in each subcell. The internal quantum efficiency (IQE) of each sub cell was set to unity, meaning that every photon absorbed in one of the layers contributes to the photocurrent density of the cell. With this IQE the electron-hole pair generation was calculated, resulting in a sub-cell specific photocurrent. With this method it is possible to calculate an unlimited amount of optical layers but it is limited by the difficulties in predicting the reflections between sub-cells. The model has been verified by comparing the calculated reflection of a single junction solar cell coated with different anti-reflection layers to the measured reflection [14].

The photocurrent densities in each subcell and the resulting photocurrent density of the quadruple solar cell are given in Table 1 for a solar cell coated with a perfect anti-reflection coating, without anti-reflection coating, with a MgF_2/ZnS double-layer anti-reflection coating, and with graded refractive index layers with parabolically increasing refractive index from 1.0 to 3.3 over a thickness of 250 nm, 500 nm, and 1000 nm. The first column in Table 1 shows the maximum photocurrent densities and the maximum efficiency of the solar cell if a perfect anti-reflection layer is used, i.e., all incident light within the absorption band of the solar cell is transmitted into and absorbed in the solar cell. The maximum photocurrent density that can be achieved when all incident light is absorbed is 13.36 mA/cm^2. When applying a graded refractive index layer with a thickness of 1000 nm and a parabolically increasing refractive index from 1 to 3.3 to the solar cell, a photocurrent density of 13.28 mA/cm^2 can be achieved. This photocurrent density is limited by the bottom cell. The calculated photocurrent density in the solar cell coated with the MgF_2/ZnS double layer anti-reflection coating is 12.54 mA/cm^2 and is in all subcells lower than the photocurrent density in the solar cell coated with the thickest graded refractive index layer. The photocurrent density in the solar cell coated with this graded refractive index layer is increased by 5.9 % with respect to that of the cell with the double layer anti-reflection coating.

3 GaP Nanowires as Anti-reflection Layers

We introduce in this section the growth of the tapered GaP nanowires on GaP and AlInP/GaAs substrates and we show the anti-reflective behavior of tapered nanowires on both substrates. We describe first the anti-reflection properties of GaP nanowires that are grown on top of a GaP substrate. As the electronic bandgap energy of GaP is 2.26 eV ($\lambda = 548$ nm) transmission and reflection measurements have been possible for wavelengths longer than 548 nm to unambiguously demonstrate

Table 1 Calculated photocurrent densities of a III/V quadruple junction solar cell coated with a perfect anti-reflection layer (AM 1.5G), different graded refractive index (GI) anti-reflection layers that have a parabolically increasing refractive index from 1.0 to 3.3 over the given thickness, a MgF$_2$/ZnS double layer anti-reflection coating with thicknesses of 89 nm (ZnS) and 105 nm (MgF$_2$) (AR layer), and a bare cell without anti-reflection layer. Table reproduced from [6].

	AM1.5G	1000 nm GI layer	500 nm GI layer	250 nm GI layer	AR layer	Bare cell
Top cell current [mA/cm^2]	16.71	13.82	13.8	13.81	12.54	10.83
Second cell current [mA/cm^2]	15.4	15.08	15.09	14.88	14.4	11.45
Third cell current [mA/cm^2]	14.98	14.94	14.9	14.16	14.72	10.86
Bottom cell current [mA/cm^2]	13.36	13.28	13.13	11.91	12.54	9.57
Resulting current [mA/cm^2]	13.36	13.28	13.13	11.91	12.54	9.57

that the tapered GaP nanowires form an anti-reflection layer. Further, we describe the growth of GaP nanowires on top of AlInP/GaAs substrates and we describe the reflection and transmission of these layers. Because of the electronic bandgap of GaAs being 1.43 eV ($\lambda = 873$ nm), transmission measurements have been only possible for wavelengths longer than 873 nm.

3.1 Growth of Tapered GaP Nanowires

GaP nanowires were fabricated using the vapor-liquid-solid (VLS) growth mechanism by metal-organic vapor phase epitaxy (MOVPE) [36]. For VLS growth, a metal catalyst particle is used to seed the growth of the nanowire underneath it. The VLS growth allows the hetero-epitaxial growth of nanowires, i.e., on a substrate of a different material than that of the nanowire. The nanowires have been grown on a double-side polished (111) GaP substrate with a thickness of 500 μm (Sample I) or on a 30 nm thick AlInP layer on top of a polished (100) n^{++}-doped GaAs wafer (Sample II). A schematic of Sample I is given in Figure 6a and in Figure 7a for Sample II. For Sample I a film of SiO$_2$ with a thickness of 500 nm was deposited on the backside of the GaP substrate to avoid etching of this surface during a surface cleaning process before the growth.

The morphology of the nanowires depends on the growth conditions and the crystallographic direction of the substrate. Conically shaped nanowires can be grown by adjusting the temperature of the substrate such that VLS and lateral growth occur simultaneously. As nanowires grow preferentially into the [111] direction [35], the nanowire growth direction can be varied by by choosing substrates with different crystallographic direction. Nanowire growth on (111) substrates results in vertically aligned nanowires, while nanowires grown on (100) substrate form an angle of 35° with the substrate. In the following, we describe the growth of nanowires on (111) GaP substrates and on (100) AlInP/GaAs substrates. The VLS growth of nanowires on (111) substrates is schematically described in Figure 6a. Gold with an equivalent

layer thickness of 0.3 nm has been evaporated on a GaP substrate. The gold-coated substrate is placed in a reactor, where it is heated in a phosphine (PH_3) atmosphere. The gold film forms small gold particles with random size distribution and position during annealing in the MOVPE reactor. The gold particles melt and form liquid droplets. When the desired growth temperature is reached, the trimethyl-gallium (TMG) is added into the reactor. The semiconductor crystal grows at the solid/liquid interface. After growth, the reactor is cooled down in a phosphine atmosphere. The initial diameter of the nanowires is determined by the size of gold particles, and thus determines the diameter at the top of the rod. When the growth temperature exceeds a critical value it is also possible to induce side-wall growth [34]. The side-wall growth of the nanowires is not catalyzed by the gold particle, therefore at low temperatures in the MOVPE reactor the sidewalls grow at a much slower rate than the VLS growth. For Samples I and II, the temperature was such that lateral growth is significant. The base of the nanowires is exposed to the side-wall growth for the longest time, therefore, the diameter is the largest at the base, and it gradually decreases toward the top of the rod. The apex angle of the conical shape can be adjusted, as the lateral growth is more pronounced with respect to the vertical growth at higher temperatures [34]. The growth parameters of both samples are given in Table 2. Figure 6b shows a scanning electron microscopy (SEM) image of Sample I. Due to tapering of the nanowires, the GaP filling fraction increases from the top to the bottom of the layer.
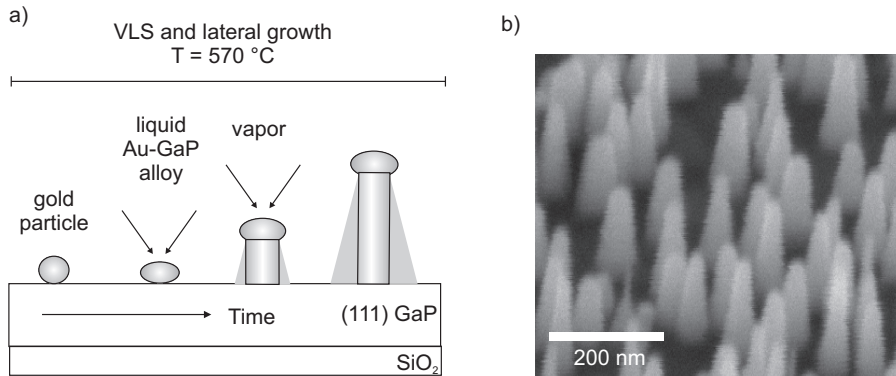

Fig. 6 a) Schematic describing the growth of the nanowires on Sample I. At a temperature of 570 °C, both VLS and lateral growth occur simultaneously resulting in tapered or conical nanowires. b) Scanning electron micrograph of Sample I.

To investigate the feasibility of nanowire graded refractive index layers on top of multijunction solar cells, layers of tapered GaP nanowires have been grown on top of AlInP. AlInP is commonly used as upper window layer in III/V solar cells [33]. For matching the growth conditions to that of a real solar cell device, 30 nm of AlInP have been grown on top of a polished (100) n^{++}-doped GaAs wafer. This AlInP layer has been protected by a 300 nm thick GaAs layer. Before nanowire growth,

this GaAs layer has been removed by etching the substrate in 28% $NH_4OH : H_2O_2 : H_2O$ (1 : 1 : 100). Immediately after this etching step, gold with an equivalent layer thickness of 0.3 nm has been evaporated and the gold coated substrate has been placed in the MOVPE reactor.

Table 2 Growth time and temperature of GaP nanowires on the given substrates. Sample I is grown on top of a GaP substrate, Sample II on top of an AlInP layer on a GaAs substrate. The averaged layer thickness is also listed. This value was obtained from SEM images.

Sample	Substrate	Growth time [s]	Growth temperature [°C]	Length [nm]
I	GaP	600	570	178 ±25
II	AlInP/GaAs	180	570	600 ±100

Considering that nanowires grow preferentially into the [111] direction [35], the orientation of the nanowires with respect to the substrate can be varied by growing them on substrates with different crystallographic orientation. On a (100) substrate, the nanowires grow preferentially with an angle of 35º with respect to the substrate surface according to the <111> direction. III/V solar cells are typically fabricated using (100) GaAs substrates. Figure 7a displays a schematic representation of the nanowire growth on a (100) substrate. The growth of nanowires on top of (100) substrates is catalyzed by a gold particle. The top diameter of the nanowires is defined by the size of this gold particle. According to the growth of Sample I, the temperature of the substrate during growth was chosen such that vertical and lateral growth occurs. Sample II is grown on an AlInP layer on top of a (100) GaAs substrate. Therefore, the nanowires on this sample grow preferentially with an angle of 35º with respect to the substrate surface. Figure 7b shows a SEM image of Sample II. The nanowires are grown epitaxially with preferential growth in the <111> direction, however, some nanowires also grow normal to the substrate. The thickness of the nanowire layer has been determined to be 600 ± 100 nm. The variation of the layer thickness can be attributed to nanowires growing into different crystallographic directions with different growth rates.

3.2 GaP Nanowires on Top of GaP Substrates

A graded refractive index layer can be achieved in ensembles of conically shaped nanowires, due to the variation of the filling fraction of GaP along the growth direction of the nanowires [7]. To determine the anti-reflection characteristics of conically shaped GaP nanowires, the broadband specular reflectance from and direct transmittance through Sample I has been measured. The reflectance has been measured at an angle of incidence of 6° with respect to the surface normal and the transmittance was measured at normal incidence. The resulting transmittance and reflectance spectra are displayed in Figures 8a and c, respectively, with blue open
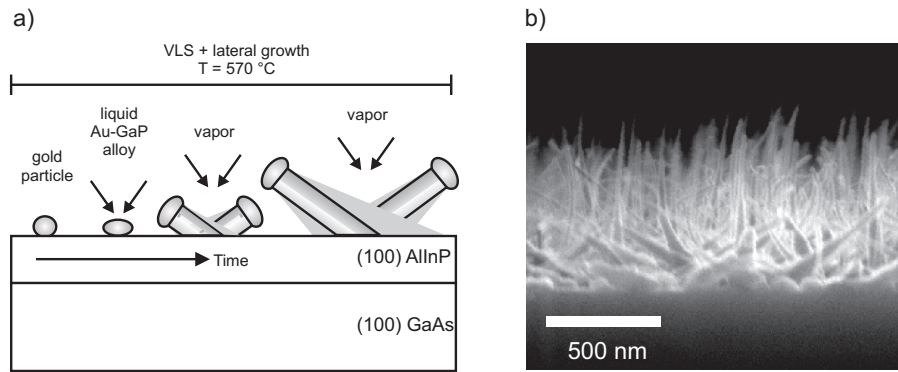
Fig. 7 a) Schematic of the growth of the nanowires on Sample II. The nanowire growth is catalyzed by a gold particle deposited on a (100) semiconductor substrate. Tapered nanowires grow under an angle of 35° with respect to the substrate at a temperature of 570 °C and the length of the nanowires is defined by the growth time. b) Cross-sectional SEM image of Sample II.

circles for Sample I. For comparison, the black solid squares show the transmittance and reflectance measurements of a bare GaP substrate with a layer of 500 nm of SiO_2 at the backside (Reference I). The sharp absorption edge at 2.26 eV ($\lambda = 548$ nm) is visible for both samples that corresponds to the electronic band gap of GaP. The small dip in the transmittance and the maximum in the reflectance of the GaP substrate around 1.76 eV ($\lambda = 700$ nm) are due to a Fabry-Pérot resonance in the SiO_2 layer at the backside of the GaP substrate. From the sum of the reflectance and transmittance measurements, the scattering losses of the samples can be estimated (see Fig. 8e). The transmittance plus reflectance is 100 % for energies below 2.26 eV for Reference I (black solid squares). As expected, there are no losses in the substrate below the band gap energy of GaP. Interband absorption has a dominant influence at higher energies.

Figure 8a reveals that the transmittance through Sample I is not increased with respect to the transmittance through the bare GaP substrate from ~ 1.88 eV ($\lambda = 660$ nm) to 2.3 eV (550 nm). At these energies, Rayleigh scattering by the nanowires reduces the transmittance and cancels its enhancement due to the anti-reflection [26]. However, the transmittance increases for lower energies as scattering losses become negligible. The transmittance of Sample I at 1.38 eV ($\lambda = 900$ nm), is increased by 20 % compared to the substrate. The small shift of the dip in transmittance (see Fig. 8a) and the peak in reflectance (see Fig. 8c) at ~ 1.85 eV (670 nm), compared to the transmittance and reflectance of Reference I, is related to a Fabry-Pérot interference in the nanowire layer, which is superimposed to the reflection in the back SiO_2 layer.

The sum of reflectance and transmittance (Fig. 8e) of Sample I (blue open circles) increases from 85 % at 2.15 eV ($\lambda = 575$ nm) to ~ 95 % at 1.38 eV ($\lambda = 900$ nm). The small reduction of the sum of reflectance and transmittance when increasing the energy can be attributed to light scattering in the nanowire layer. The enhanced transmittance measurements of Figure 8a demonstrate that the reduction in specular
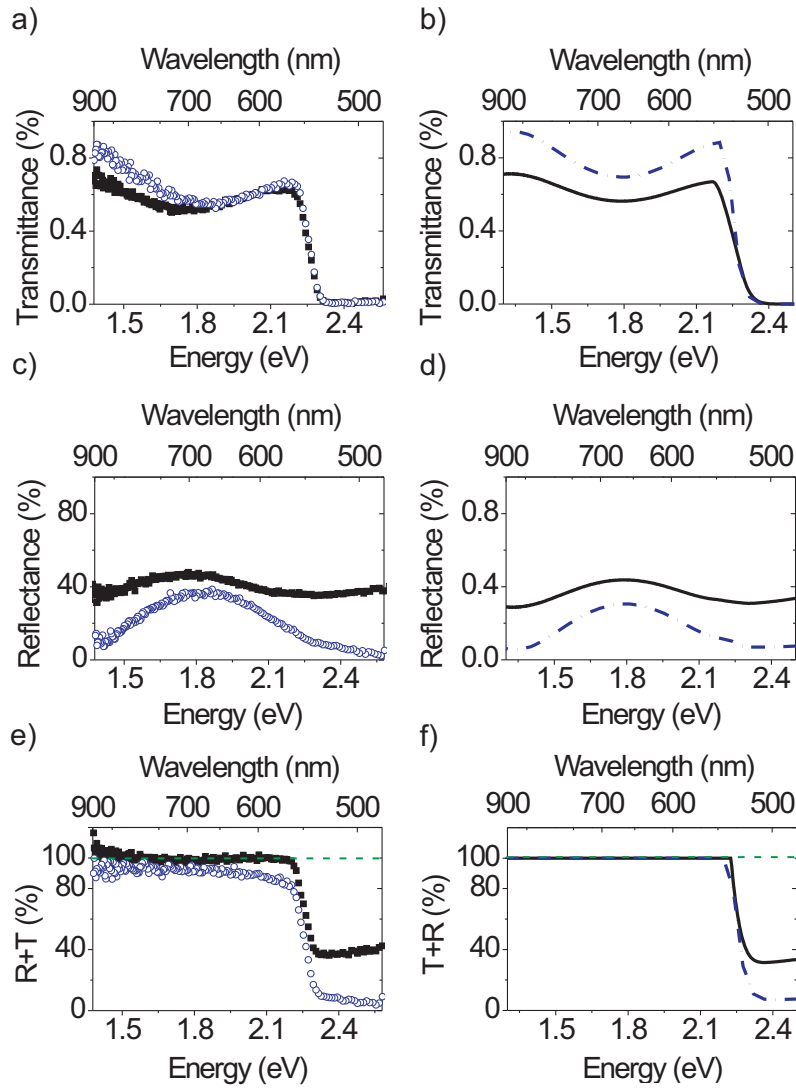
Fig. 8 a) Measured transmittance and b) calculated transmittance for normal incidence, c) measured reflectance and d) calculated reflectance at an angle of incidence of 6°, e) the sum of measured reflectance and transmittance, and f) the sum of calculated reflectance and transmittance. The measurements (calculations) for a bare GaP substrate with one side covered by a 500 nm (490 nm) layer of SiO$_2$ are shown as black squares (black solid curve). The blue circles (blue dashed-dotted curve) correspond to the measurements (calculations) of Sample I. (Fig. reproduced from [7].)

reflectance reported in Figure 8c is not only due to surface roughness or scattering in the nanowire layer, but also to the refractive-index matching that the nanowire layer provides between air and GaP.

Figure 8b, d, and f show calculations of the transmittance and reflectance, of Sample I (blue dashed-dotted curve) and a bare GaP substrate covered on one side with a SiO_2 layer with a thickness of 490 nm (black solid curve). These calculations have been performed with the transfer-matrix method described in Section 2. The calculated system consists of five layers: air, nanowire layer, GaP substrate, SiO_2, and air. The nanowire layer is sliced into 50 horizontal sublayers, each of them having a thickness of 5 nm. For Sample I a quadratically increase of the refractive index per sublayer with the length of the nanowires has been assumed. This quadratic increase is based on the assumption that the filling fraction is proportional to the square of the diameter of the nanowires, and that the effective refractive index is proportional to the GaP filling fraction. From the calculations, a variation of the refractive index over the nanowire layer length from 1.1 up to 2.1 has been determined. The calculations (Figs. 8b, d, and f) show the same trend as the measurements (Figs. 8a, c, and e). The small discrepancies can be attributed to the aforementioned scattering, which is not included in the calculations. Both measurement and calculation show a reduction for the sum of transmittance and reflectance (Figs. 8e and f) with respect to the bare GaP substrate for energies higher than the electronic band gap of GaP. This reduction can be attributed to an enhanced absorption in GaP due to the anti-reflection coating.
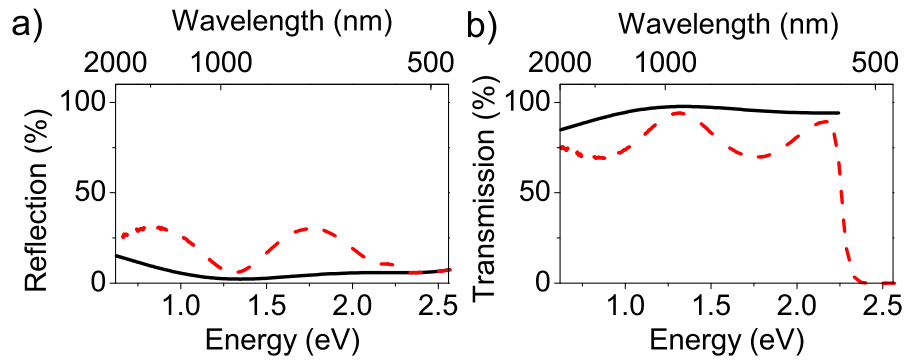

Fig. 9 a) Calculated reflectance and b) transmittance for a graded refractive index layer with a parabolically increasing refractive index on top of an infinite GaP substrate (black solid curve) and on a 500 μm thick GaP substrate with a 490 nm thick SiO_2 layer on the backside (red dashed curve). The graded index layer has a thickness of 250 nm and the refractive index is varied from 1.1 at the top to 2.1 at the bottom.

To determine the effect of the anti-reflection layer independently from the reflections in the substrate, calculations of the reflectance from and transmittance through a nanowire layer on top of an infinitely thick GaP substrate (black solid curves, Fig. 9) have been performed. These calculations are compared in Figures 9a and b

to the reflectance from and transmittance through a similar nanowire layer on top of a 500 μm thick GaP substrate covered with 490 nm SiO$_2$ on the backside (red dashed curves). While there is a minor oscillation visible in the calculation assuming an infinite substrate, the calculations of the same anti-reflection layer on top of 500 μm GaP covered with 490 nm of SiO$_2$ on the backside show large variations in the transmittance and reflectance as a function of wavelength. Comparing both calculations, it can be concluded that the modulation of the transmittance and reflectance through Sample I are due to Fabry-Pérot resonances in the SiO$_2$ layer in the bottom of the wafer and on the nanowire film on top. The minor oscillations in the calculation of the anti-reflection layer on top of the infinitely thick GaP substrate, indicates that the nanowire layer acts both as a graded-refractive-index coating and a single-layer interference coating.

3.3 Tapered GaP Nanowires on AlInP/GaAs Substrates

We have shown in the previous section that tapered GaP nanowires form a graded refractive index layer that increases light coupling into a GaP substrate. Here, we show that GaP nanowires on top of an AlInP/GaAs substrate similarly reduce the reflection from and increase the transmission through an AlInP/GaAs substrate. While it has been possible to measure the transmission through the nanowire layer on top of a GaP substrate for wavelengths as low as 550 nm, the transmission can only be measured for wavelengths longer than 873 nm when the nanowires are on top of an AlInP/GaAs substrate. For wavelengths shorter than 873 nm, the incident light is fully absorbed in the GaAs substrate and no light is transmitted.

To demonstrate that GaP nanowires on top of an AlInP/GaAs substrate form a graded refractive index layer, measurements of the angle-integrated reflection from and transmission through the AlInP/GaAs substrate (Reference II) and the AlInP/GaAs substrate coated with tapered nanowires (Sample II) have been done. The total reflectance and transmittance has been measured for wavelengths between 350 nm and 2000 nm using the integrating sphere PerkinElmer Lambda 950 commercial setup. The PerkinElmer Lambda 950 spectrometer consists of a tungsten-halogen and a deuterium lamp, in combination with an integrating sphere, a photomultiplier for visible, and a PbS detector for infrared light. The working principle of an integrating sphere is described in Figure 10a in transmission and in Figure 10b in reflection. For the transmittance measurements, the sample was mounted in front of the integrating sphere, so that all transmitted light was collected, that is the zeroth-order and diffusely transmitted light. For the reflectance measurements, the sample was mounted at the backside of the integrating sphere with its surface normal at an angle of 8° with respect to the incident light beam, so that all the reflected light from the sample could be collected and detected. The integrating sphere is coated at the inside with a diffusive coating. Specularly reflected or transmitted light and the diffusely reflected or transmitted light are randomized and the intensity is equally distributed over the sphere. Measuring the intensity on each point of the sphere will

lead to the same result. The diffusely reflected light is measured by making a small opening in the integrating sphere in such a way that the specularly reflected light escapes from the sphere. The reflection measurements on the samples are normalized by the reflection of a white-standard to obtain the absolute reflectance of the sample. From the total reflectance, R, and the diffuse reflectance, R_{dif}, the specular reflectance, R_{spec}, can be determined by $R_{\mathrm{spec}} = R - R_{\mathrm{dif}}$. Measuring the reflection with an integrating sphere is a good technique for determining the characteristics of nanostructured anti-reflection coatings on top of absorbing substrates. As the specularly and diffusely reflected light can be determined independently, anti-reflective and scattering properties of the nanostructures can be determined independently.

The measured total reflectance (black squares), diffuse reflectance (red circles), and the resulting specular reflectance (blue triangles) from Reference II are displayed in Figure 11a. At wavelengths below the electronic bandgap of GaAs (873 nm) the total and specular reflectance are similar (28 %) and the diffuse reflectance is negligible. This low diffuse reflectance is expected for a flat layer. For wavelengths longer than 873 nm, the reflectance increases to 36 %, as the reflectance of the backside of the substrate is contributing to the measurement. At these wavelengths, the diffuse reflectance is slightly increased, indicating that the backside of the sample is rougher than the front side. From these two measurements, the contribution to the reflection of the substrate backside and the AlInP front side of the sample can be understood.
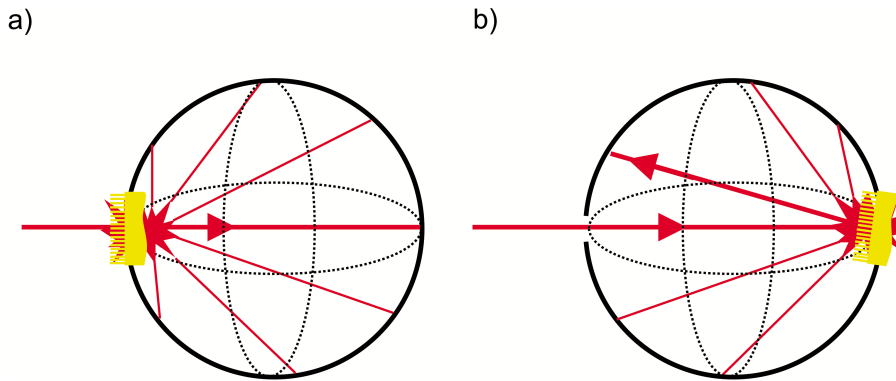
a)   b)

Fig. 10 Schematic of the integrating sphere used for a) total transmittance measurements and b) for total reflectance measurements. The direct transmitted or reflected beam and the diffuse transmitted or reflected beam can be measured simultaneously by using the integrating sphere. For the reflectance measurement, the sample is mounted with an angle of 8° with respect to the incident light so that the specularly reflected beam does not escape from the sphere.

Additionally, the total and diffuse reflectance from Sample II have been measured. These measurements are displayed in Figure 11b. The total reflectance (black squares) is strongly reduced compared to the measurement of the AlInP/GaAs substrate. While the total reflectance is lower than 10 % at wavelengths below 873 nm, the total reflectance increases for wavelengths above the electronic bandgap of GaAs
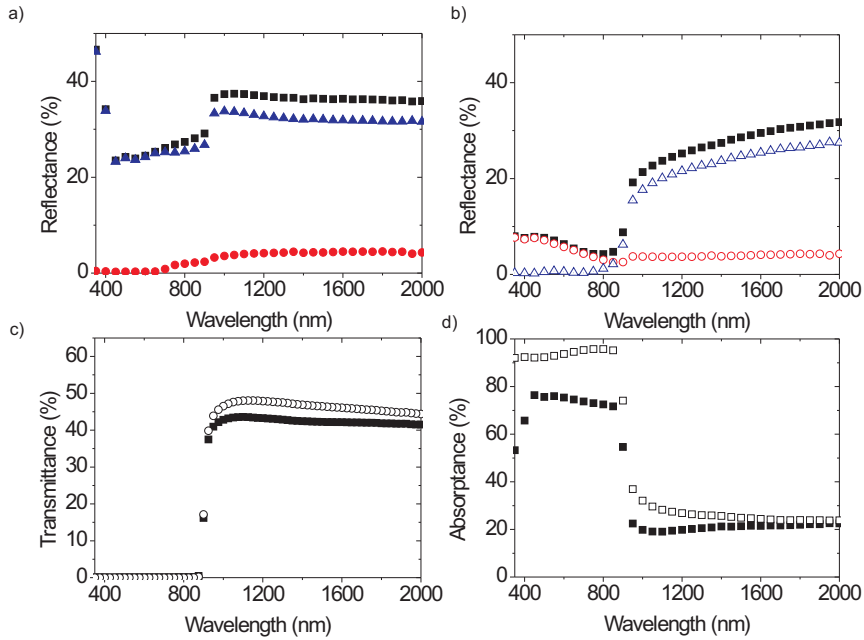
Fig. 11 a) Measured reflectance from the AlInP/GaAs substrate and b) measured reflectance from the AlInP/GaAs substrate coated with tapered nanowires. In both graphs the total reflectance (black squares), specular reflectance (blue triangles), and diffuse reflectance (red circles) are displayed. c) Measured total transmittance through and d) measured absorptance in the AlInP/GaAs substrate (solid circles) and the AlInP/GaAs substrate coated with tapered nanowires (open circles). (Fig. reproduced from [6])

as in the case of the bare AlInP/GaAs substrate. This increased total reflectance can be attributed to the reflectance of the backside of the substrate. The diffuse reflectance (red circles) is dominating the total reflectance for wavelengths shorter than 873 nm. The increasing diffuse reflectance with decreasing wavelength is due to scattering of light from the thick bottom part of the nanowires [26]. For wavelengths longer than 865 nm, the diffuse reflectance is similar to that of the AlInP/GaAs substrate, indicating that scattering of light from the nanowires is negligible at these wavelengths.

Although these first measurements have demonstrated that the reflectance of the AlInP/GaAs substrate coated with tapered nanowires is significantly reduced with respect to the bare AlInP/GaAs substrate, the reflectance of the nanowire sample needs to be further decreased for a perfect anti-reflection coating. Therefore, a smaller gradient of the refractive index has to be realized. Further, the bottom diameter of the nanowires has to be decreased to reduce the diffuse reflection at short wavelengths and the density of nanowires has to be increased to achieve a high index of refraction at the interface with the AlInP.

To determine the enhancement of the coupling of light into the AlInP/GaAs substrate by the tapered nanowires, the total transmittance through Reference II (solid circles in Figure 11c) and through Sample II (open circles) have been measured. For wavelengths below 873 nm, the transmission is negligible in both measurements, as the light is absorbed in the 360 μm thick GaAs substrate. For wavelengths above the electronic bandgap of GaAs ($\lambda = 873$ nm), the transmittance through the bare AlInP/GaAs substrate increases strongly, reaching 43 % for wavelengths longer than 950 nm. The transmittance through Sample II is 47 %. The transmittance through Sample II and Reference II are influenced by residual free-carrier absorption for wavelengths above the electronic bandgap of GaAs, which also causes the rather low increase of the transmittance through Reference II coated with nanowires with respect to the bare AlInP/GaAs substrate. This residual absorptance A can be determined by $A = 100\% - R - T$, with R and T being the total reflectance and transmittance, respectively. The absorptance in Reference II and in Sample II are displayed in Figure 11d. The absorption in the nanowire coated sample (open squares) is increased with respect to the uncoated substrate (solid squares) for all wavelengths. For the wavelength range below 873 nm, the fact that less light is reflected is the main cause for the enhanced absorption (absorptance higher than 90%) in the sample coated with nanowires. For the wavelength range above 873 nm, the increased absorption might be attributed to diffusely transmitted light due to the nanowires. The diffusely transmitted light travels through the GaAs with a longer optical path length, resulting in a higher absorption probability due to free-carrier absorption.

The desired anti-reflection coating should omnidirectionally reduce the reflection and increase the transmission into the solar cell because multi-junction solar cells are usually installed in concentrator systems. To determine the angle-dependence of the response of the anti-reflection layer, the zero-order transmission through Sample II and Reference II have been measured for angles of incidence from 0° to 55° using unpolarized light. Figure 12 displays the transmission through Sample II normalized to the transmission through Reference II. For all wavelengths and angles, the normalized transmission is above unity, meaning that for all wavelengths and angles, the transmission into the AlInP/GaAs layer is increased by the presence of the nanowire layer. The insets in Figure 12 show cuts to the measurement at a wavelength of 1300 nm as a function of angle of incidence, and at an angle of incidence of 25° as a function of wavelength. These cuts show that overall the transmission is increased by around 20 %. In a Fresnel lens based concentrator system the light is typically incident over angles from 0° to 30°, however, higher angles of incidence would allow thinner concentrator modules.

Solar cells that are installed in concentrator systems have to be robust to high irradiance levels. To determine if the nanowire layer is stable under concentrated sunlight, the Sample II has been illuminated with 125 suns (AM1.5G) for 4 hours. During the illumination, the sample was mounted on a Cu base for temperature control and the temperature of the sample was kept at 50 °C. The reflection before and after illumination on 5 different positions of the sample has been measured, and no significant difference between the measurements has been found. From the
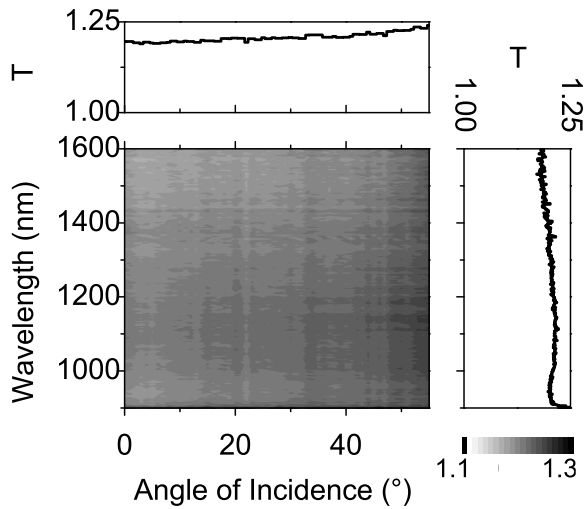
Fig. 12 Measured transmission through the AlInP/GaAs substrate coated with nanowires normalized to the transmission through an AlInP/GaAs substrate as a function of angle of incidence and wavelength. The top inset shows a cut to the measurement at 1300 nm and the right inset shows a cut at an angle of incidence of 25°. (Fig. reproduced from [6])

reflection measurements before and after illumination with 125 suns, it has been concluded that the nanowire layer is stable under concentrated sunlight.

4 Conclusions

In conclusion, we have described the anti-reflective properties of layers of GaP nanowires. These anti-reflective properties have been determined by wavelength- and angle-dependent transmittance and reflectance measurements. The reflectance and transmittance of graded refractive index layers are described quantitatively using a transfer-matrix method for isotropic layered media. We have presented calculations showing that the photocurrent density of a III/V quadruple solar cell can be increased when applying a graded refractive index coating to the solar cell instead of the standard MgF_2/ZnS double layer anti-reflection coating.

GaP nanowires have been fabricated by metal organic vapor phase epitaxy using the VLS mechanism and we have shown that the enhanced transmittance and corresponding reduced reflectance of these layers is related to a graded refractive index in the nanowire layer. The enhanced direct transmittance show that scattering and absorption are weak in these layers.

For demonstrating the feasibility of graded refractive index layers on solar cells, layers of tapered GaP nanowires on AlInP/GaAs substrates have been grown and the transmission and reflection properties of these layers have been investigated.

The reflection from AlInP/GaAs substrates can be reduced by coating the substrate with a graded refractive index layer. The described experiments reveal that the total reflection is indeed reduced over a broad spectral range when applying tapered GaP nanowires on top of an AlInP/GaAs substrate and that the transmission into the substrate is increased for a wide spectral and angular range. These results render tapered nanowires a promising candidate for increasing the efficiency of III/V multi-junction solar cells.

References

1. Bernhard, C.G.: Structural and functional adaption in a visual system. Endeavour **26**, 79 (1967)
2. Born, M., Wolf, E.: Principles of optics, 6th edn. Cambridge University Press (1997)
3. Chattopadhyay, S., Huang, Y.F., Jen, A.J., Ganguly, A., Chen, K.H., Chen, L.C.: Anti-reflecting and photonic nanostructures. Materials Science and Engineering **R 69**, 1–35 (2010)
4. Chiu, C.H., Yu, P., Kuo, H.C., Chen, C., Lu, T.C., Wang, S., Hsu, S.H., Cheng, Y.J., Chang, Y.C.: Broadband and omnidirectional antireflection employing disordered GaN nanopillars. Optics Express **16**, 8748–8754 (2008)
5. Clapham, P.B., Hutley, M.C.: Reduction o lens reflexion by the "moth eye" principle. Nature **224**, 281–282 (1973)
6. Diedenhofen, S.L., Grzela, G., Haverkamp, E., Bauhuis, G., Schermer, J., Gómez Rivas, J.: Broadband and omnidirectional anti-reflection layer for III/V multi-junction solar cells. Solar Energy Materials and Solar Cells **101**, 308–314 (2012)
7. Diedenhofen, S.L., Vecchi, G., Algra, R.E., Hartsuiker, A., Muskens, O.L., Immink, G., Bakkers, E.P.A.M., Vos, W.L., Gmez Rivas, J.: Broad-band and omnidirectional antireflection coatings based on semiconductor nanorods. Adv. Mat. **21**, 973–978 (2009)
8. Dobrowolski, J.A., Poitras, D., Ma, P., Vakil, H., Acree, M.: Toward perfect antireflection coatings: numerical investigation. Appl. Opt. **41**(16), 3075–3083 (2002)
9. Friedman, D.: Progress and challenges for next-generation high-efficiency multijunction solar cells. Current Opinion in Solid State and Materials Science **14**, 131 – 138 (2010)
10. Gombert, A., Glaubitt, W., Rose, K., Dreibholz, J., Bläsi, B., Heinzel, A., Sporn, D., Döll, W., Wittwer, V.: Subwavelength-structured antireflective surfaces on glass. Thin Solid Films **351**, 73–78 (1999)
11. Grann, E.B., Moharam, M.G., Pommet, D.A.: Optimal design for antireflective tapered two-dimensional subwavelength grating structures. J. Opt. Soc. Am. A **12**, 333–339 (1995)
12. Green, M.A., Emery, K., Hishikawa, Y., Warta, W., Dunlop, E.D.: Solar cell efficiency tables (version 41). Progress in Photovoltaics: Research and Applications **21**(1), 1–11 (2013). DOI 10.1002/pip.2352. URL http://dx.doi.org/10.1002/pip.2352
13. Guter, W., Schne, J., Philipps, S.P., Steiner, M., Siefer, G., Wekkeli, A., Welser, E., Oliva, E., Bett, A.W., Dimroth, F.: Current-matched triple-junction solar cell reaching 41.1 % conversion efficiency under concentrated sunlight. Appl. Phys. Lett. **94**, 223,504 (2009)

14. Haverkamp, E.J., Mulder, P., Bauhuis, G.J., Schermer, J.J., Voncken, M.M.A.J., van Deelen, J., van Niftrik, A.T.J., Larsen, P.K.: Spectrum and bandgap optimized antireflection coating by numerical simulations. In: 20th European Photovoltaic Solar Energy Conference (2005)
15. Hobbs, D.S., MacLeod, B.D., Riccobono, J.R.: Update on the development of high performance anti-reflecting surface relief micro-structures. Proc. of SPIE **6545**, 65,450Y (2007)
16. Huang, Y.F., Chattopadhyay, S., Jen, Y.J., Peng, C.Y., Liu, T.A., Hsu, Y.K., Pang, C.L., Lo, H.C., Hsu, C.H., Chang, Y.H., Lee, C.S., Chen, K.H., Chen, L.C.: Improved broadband and quasi-omnidirectional anti-reflection properties with biomimetic silicon nanostructures. Nat. Nanotech. **2**, 770–774 (2007)
17. Kanamori, Y., Sasaki, M., Hane, K.: Broadband antireflection gratings fabricated upon silicon substrates. Opt. Lett. **24**, 1422–1424 (1999)
18. Kikuta, H., Toyota, H., Yu, W.: Optical elements with subwavelength structured surfaces. Optical Review **10**, 63–73 (2003)
19. King, R.R., Law, D.C., Edmondson, K.M., Fetzer, C.M., Kinsey, G.S., Yoon, H., Krut, D.D., Ermer, J.H., Sherif, R.A., Karam, N.H.: Advances in high-efficiency III-V multijunction solar cells. Advances in OptoElectronics **2007**, 29,523 (2007)
20. King, R.R., Law, D.C., Edmondson, K.M., Fetzer, C.M., Kinsey, G.S., Yoon, H., Sherif, R.A., Karam, N.H.: 40% efficient metamorphic GaInP/GaInAs/Ge multijunction solar cells. Appl. Phys. Lett. **90**, 183,516 (2007)
21. Laff, R.A.: Silicon nitride as an antireflection coating for semiconductor optics. Appl. Opt. **10**(4), 968–969 (1971). URL http://ao.osa.org/abstract.cfm?URI=ao-10-4-968
22. Lalanne, P., Morris, G.M.: Antireflection behaviour of silicon subwavelength periodic structures for visible light. Nanotechnolgy **8**, 53–56 (1997)
23. Law, D.C., King, R., Yoon, H., Archer, M., Boca, A., Fetzer, C., Mesropian, S., Isshiki, T., Haddad, M., Edmondson, K., Bhusari, D., Yen, J., Sherif, R., Atwater, H., Karam, N.: Future technology pathways of terrestrial III-V multijunction solar cells for concentrator photovoltaic systems. Solar Energy Materials and Solar Cells **94**(8), 1314 – 1318 (2010)
24. Lee, Y.J., Ruby, D.S., Peters, D.W., McKenzie, B.B., Hsu, J.W.P.: ZnO nanostructures as efficient antireflection layers in solar cells. Nano Lett. **8**, 1501 (2008)
25. Lohmüller, T., Helgert, M., Sundermann, M., Brunner, R., Spatz, J.P.: Biomimetic interfaces for high-performance optics in the deep-uv light range. Nano Lett. **8**, 1429 (2008)
26. Muskens, O.L., Diedenhofen, S.L., van Weert, M.H.M., Borgström, M.T., Bakkers, E.P.A.M., Gómez Rivas, J.: Epitaxial growth of aligned semiconductor nanowire metamaterials for photonic applications. Adv. Func. Mat. **18**, 1039 (2008)
27. Poitras, D., Dobrowolski, J.A.: Toward perfect antireflection coatings. 2. theory. Appl. Opt. **43**(6), 1286–1295 (2004)
28. Rayleigh, L.: On reflection of vibrations at the confines of two media between which the transition is gradual. Proceedings of the London Mathematical Society **s1-11**(1), 51–56 (1879)
29. Southwell, W.H.: Gradient-index antireflection coatings. Opt. Letters **8**(11), 584–586 (1983)
30. Stan, M., Aiken, D., Cho, B., Cornfeld, A., Ley, V., Patel, P., Sharps, P., Varghese, T.: High-efficiency quadruple junction solar cells using OMVPE with inverted metamorphic device structures. Journal of Crystal Growth **312**, 1370 – 1374 (2010)
31. Sun, C.H., Jiang, P., Jiang, B.: Broadband moth-eye antireflection coatings on silicon. Appl. Phys. Lett. **92**, 061,112 (2008)
32. Sun, C.H., Min, W.L., Linn, N.C., Jiang, P.: Templated fabrication of large area subwavelength antireflection gratings on silicon. Appl. Phys. Lett. **91**, 231,105 (2007)
33. Tommila, J., V.Polojärvi, A.Aho, A.Tukiainen, J.Viheriälä, J.Salmi, A.Schramm, J.M.Kontio, Turtiainen, A., T.Niemi, M.Guina: Nanostructured broadband antireflection coatings on AlInP fabricated by nanoimprint lithography. Solar Energy Materials and Solar Cells **94**, 1845 1848 (2010)
34. Verheijen, M.A., Immink, G., de Smet, T., Borgström, M.T., Bakkers, E.P.A.M.: Growth kinetics of heterostructured GaP-GaAs nanowires. JACS **128**, 1353 – 1359 (2006)
35. Wacaser, B.A., Dick, K.A., Johansson, J., Borgström, M.T., Deppert, K., Samuelson, L.: Preferential interface nucleation: An expansion of the VLS growth mechanism for nanowires. Adv. Mat. **21**, 153–165 (2009)

36. Wagner, R.S., Ellis, W.C.: Vapor-liquid-solid mechanism of single crystal growth. Appl. Phys. Lett. **4**, 89–90 (1964)
37. Xi, J.Q., Schubert, M.F., Kim, J.K., Schubert, E.F., Chen, M., Lin, S.Y., Liu, W., Smart, J.A.: Optical thin-film materials with low refractive index for broadband elimination of fresnel reflection. Nat. Photonics **1**, 176–179 (2007)
38. Yan, X., Poxson, D.J., Cho, J., Welser, R.E., Sood, A.K., Kim, J.K., Schubert, E.F.: Enhanced omnidirectional photovoltaic performance of solar cells using multiple-discrete-layer tailored- and low-refractive index anti-reflection coatings. Adv. Func. Mat. **23**, 583–590 (2013)
39. Yeh, P.: Optical waves in layered media. John Wiley and Sons, New York, Chichester, Brisbane, Toronto, Singapore (1988)
40. Yu, Z., Gao, H., Ge, H., Chou, S.Y.: Fabrication of large area subwavelength antireflection structures on Si using trilayer resist nanoimprint lithography and liftoff. J. Vac. Sci. Technol. B **21**, 2874–2877 (2003)
41. Zhou, W., Tao, M., Chen, L., Yang, H.: Microstructured surface design for omnidirectional antireflection coatings on solar cells. J. Appl. Phys. **102**, 103,105 (2007)
42. Zhu, J., Yu, Z., Burkhard, G.F., Hsu, C.M., Connor, S.T., Xu, Y., Wang, Q., McGehee, M., Fan, S., Cui, Y.: Optical absorption enhancement in amorphous silicon nanowire and nanocone arrays. Nano Lett. **9**, 279–282 (2009)